Chemical Engineering Journal 519 (2025) 165496

Contents lists available at ScienceDirect

Chemical Engineering Journal

journal homepage: www.elsevier.com/locate/cej

3D printing of flash graphene/nano-cellulose aerogel for high-efficiency solar evaporation with superior salt resistance

Zhigang Wang [a], Chunjie Yan [a], Kaiyue Ji [a], Jun Cao [a], Yang Chen [a], Yuting Gao [a], Heng Deng [a,b,*]

[a] Faculty of Materials Science and Chemistry, China University of Geosciences, Wuhan 430074, PR China
[b] Shenzhen Research Institute, China University of Geosciences, Shenzhen 518000, PR China

ARTICLE INFO

Keywords:
3D printing
Double-layer structure
Nanocellulose scaffold
Interface evaporation
Flash graphene

ABSTRACT

Solar-driven evaporation is a promising approach for seawater desalination, but challenges such as salt accumulation and limited evaporation efficiency persist. This study presents a 3D-printed flash graphene (FG) composite nano-cellulose aerogel for solar evaporators. FG, a small-sized, turbostratic graphene nanoflake produced via Flash Joule Heating (FJH), is integrated into cellulose-based printable inks to enhance photothermal performance without compromising ink stability or the aerogel's porous structure. The resulting Janus-structured aerogel features a localized FG photothermal layer placed on a hierarchical, interconnected porous scaffold, created through multi-material 3D printing. This design minimizes heat loss by isolating the photothermal layer from the water source, ensuring efficient thermal conversion. The scaffold's inherent porosity and wicking channels facilitate rapid water transport, while also promoting effective salt circulation and preventing crystallization on the evaporative surface. The composite aerogel demonstrates high evaporation efficiency and superior salt resistance, positioning it as a promising material for sustainable solar desalination applications. This work provides an effective approach for developing advanced, high-performance solar evaporators with enhanced longevity.

1. Introduction

The scarcity of freshwater resources is a critical challenge facing the global community, driving an urgent demand for sustainable solutions to seawater desalination [1]. Solar-driven evaporation technologies represent a promising approach for converting seawater into potable water using clean, renewable energy [2]. Solar-driven evaporators harness sunlight to heat seawater and facilitate water evaporation while leaving salts and other impurities behind [3]. These evaporators are typically composed of photothermal materials embedded within a hydrophilic scaffold [4,5]. Photothermal materials, such as graphene [6,7], liquid metals [8], metal oxides [9], and compounds like MoS_2 [10], play a pivotal role by converting absorbed light into thermal energy, thus promoting efficient water evaporation. Meanwhile, hydrophilic scaffolds act as capillary pumps, drawing water from the bulk reservoir to the photothermal surface, where evaporation occurs.

To enhance solar evaporation rates, hydrophilic materials such as hydrogels and aerogels have been developed as scaffolds, leveraging their porous polymeric networks to facilitate water transport. Hydrogels and aerogels composed of synthetic polymers like PVA [11], PAAc [12], PAAm [13], or natural biopolymers such as cellulose [14], alginate [15], and starch [16], are particularly effective. These scaffolds alter the interaction between their hydrophilic networks and water molecules, enabling a reduction in the vaporization enthalpy of water. This design allows solar evaporators to achieve high evaporation efficiencies, even under diffuse sunlight, by efficiently utilizing low-intensity solar energy [17]. However, high evaporation rates alone are insufficient for practical desalination applications, as effective salt resistance is equally essential. Rapid evaporation can lead to salt accumulation on the evaporative surface, causing crystallization that reduces both the efficiency and longevity of the device [18,19]. An effective strategy to mitigate salt buildup is to enhance the salt circulation within the scaffold, promoting an equilibrium between water evaporation and salt diffusion [20]. The introduction of 3D printing technology offers a means to optimize the design of evaporator scaffolds for both rapid water supply and effective salt circulation. By incorporating

* Corresponding author at: Faculty of Materials Science and Chemistry, China University of Geosciences, Wuhan 430074, PR China.
E-mail address: dengheng@cug.edu.cn (H. Deng).

https://doi.org/10.1016/j.cej.2025.165496
Received 30 April 2025; Received in revised form 20 June 2025; Accepted 29 June 2025
Available online 30 June 2025

interconnected wicking channels through 3D printing, evaporators can improve water delivery to the photothermal surface while maintaining continuous salt circulation [21]. Moreover, the channel geometry created by 3D printing induces multiple internal light reflections, boosting overall light absorption and photothermal efficiency [22].

Despite the advantages of structured 3D-printed scaffolds, developing an optimal ink composition for 3D printing remains a complex challenge. Achieving printability, ink stability, and appropriate pore-forming properties require careful consideration, often involving iterative adjustments. In certain cases, machine learning algorithms are employed to streamline the formulation process [23,24]. To achieve effective solar evaporation, photothermal materials must be incorporated into the printable ink, which introduces additional design complexities. For instance, some photothermal agents, such as liquid metals, tend to deposit unevenly, resulting in inhomogeneous final structures [25]. Large size photothermal materials, like graphene and MXene, can compromise the porous architecture of the printed scaffold [26]. Furthermore, many photothermal materials are inherently hydrophobic and require chemical modifications to disperse well within aqueous inks. For instance, the hydrophobic nature of pristine graphene hinders its uniform dispersion in water, while the use of reduced graphene oxide introduces additional oxidation-reduction steps, complicating the process [26]. In addition, multi-material printing techniques are often required to produce Janus-structured evaporators, where one side of the structure contains photothermal agents while the other does not. Such designs help localize heat generation and minimize heat loss by reducing direct contact between the photothermal layer and the water source [27,28]. However, achieving a well-defined Janus structure requires that the addition of photothermal agents minimally impact the ink's printability and structural properties. Ideally, a photothermal agent should impart high photothermal efficiency to the ink without compromising its stability, printability, or porous network characteristics.

In this study, a novel photothermal agent, Flash Graphene (FG), is introduced to address these challenges. FG is fabricated via an environmentally friendly and cost-effective Flash Joule Heating (FJH) technique, which produces a unique, small-sized turbostratic graphene nanoflake [29–31].

FG demonstrates exceptional photothermal properties, enabling significant enhancement of the cellulose aerogel's photothermal performance with the addition of just 0.08 wt%. Owing to its turbostratic structure and small size, FG disperses readily in aqueous solutions and is well-suited for inclusion in cellulose-based printable inks. Notably, the addition of FG does not compromise the ink's printability or alter the porous structure of the resultant cellulose aerogel. By employing multi-material 3D printing, a Janus-structured FG/cellulose aerogel is fabricated, incorporating a localized photothermal layer within a hierarchical porous scaffold. This Janus design effectively prevents direct contact between the photothermal layer and the water source, minimizing heat loss through diffusion and improving overall thermal efficiency. The hierarchical structure comprises the inherent porosity of the cellulose scaffold as well as interconnected wick channels formed during 3D printing. These structural features facilitate rapid water transport, effective thermal isolation, and efficient diffusion and convection of salt ions, resulting in a solar evaporator with both high evaporation efficiency and enhanced salt resistance.

2. Experimental section

2.1. Materials

Cellulose nanofibers (CNF, 4.5 wt%, solid content) were purchased from Zhongshan Nanofiber New Materials Co., Ltd. Sodium carboxymethyl cellulose (CMC) and citric acid monohydrate (CA) was purchased from Shanghai Sinopharm group. Carbon black was offered by Tianjin Huayuan Chemical Technology Co., Ltd. Deionized (DI) water was came from Laboratory of China University of Geosciences (Wuhan).

2.2. Preparation of 3D printing ink

CNF-based composite ink for 3D printing was prepared according to the following steps. A total of 1.2 g of CMC was slowly added to CA solutions prepared at different concentrations (0.1, 0.2, and 0.4 g/g), with continuous stirring to ensure full dissolution. Subsequently, 6.65 g of CNF was introduced into the mixture under vigorous agitation. (4.5 wt%, solid content). The solution was evenly stirred with an iron spoon until no more CNF fibers are visible. Then the ink was covered with aluminum foil and was stored in a refrigerator at 2–8 °C for further use. FG/CNF printing ink was prepared using the same method. Firstly, FG solutions of varying concentrations were prepared (the synthesis procedure of FG follows the method reported in our earlier publication [32]). FG solutions at concentrations of 1, 2, 3, and 4 mg/mL were prepared by dispersing 5, 10, 15, and 20 mg of FG in 5 mL of deionized water containing 5 mg of polyether F-188 (A nonionic amphiphilic surfactant, stabilizes the dispersion by its hydrophobic PPO segments interacting with FG surfaces and hydrophilic PEO chains ensuring compatibility with the aqueous phase [31]). Then, the solution was dispersed evenly using ultrasound with ultrasonic processor (FS-1200 N, SXSONIC, 1200 w), and the FG solution was added to the aforementioned ink formula to ensure that the solid content of the ink matched that of pure CNF ink.

2.3. Preparation of the Janus FG/CNF aerogel

Before printing, the ink was equilibrated to room temperature to ensure consistent rheological behavior. Subsequently, it was printed using a 3D printing system (Adventure 3D-LB-Printer-0100). Pure CNF ink and FG/CNF ink were loaded into plastic syringes for dual-nozzle printing, with a needle diameter of 260 μm. An acrylic plate was used as the printing substrate, and the Y-offset was set to −0.5 mm, X-offset to 64 mm, the height of each printed layer was set to 200 μm, and printing speed to 6 mm/s. AutoCAD was utilized to design and export DXF files for integration into the printing system. Twenty layers of CNF were initially printed, upon which ten layers of FG/CNF composite were subsequently deposited. The thickness ratio between the FG/CNF photothermal layer and the CNF supporting layer is 1:2 (Fig. S1). All printed samples were frozen in a refrigerator at −25 °C for 12 h, then freeze-dried for 10 h. The samples were then placed in a glass container, completely covered with aluminum foil, and stored in a vacuum oven (120 °C) for 24 h. Chemical crosslinking was achieved through dehydrogenation heat treatment (DHT) to obtain the Janus FG/CNF aerogel. The CNF scaffolds and FG/CNF scaffolds were also prepared using the same method. The sample used for measuring the contact angle was prepared using the mold method, further drying and cross-linking will be carried out (Fig. S2).

2.4. Characterization and measurement

Transmission Electron Microscope (TEM, Philips company, Holland) was utilized to observe the morphology of CNF, while Field Emission Scanning Electron Microscope (FESEM, Hitachi SU8010) was employed to examine the microstructure of aerogel. A Rotational Rheometer was used to characterize the rheological properties of 3D printing ink. UV–Vis-NIR Spectrophotometer (Shimadzu-UV300) was utilized to measure the absorption spectrum of materials. The contact angle was determined using a Contact Angle Meter (OCA, JC2000D1).

2.5. Measurement of mechanical properties of aerogel

A sample with a thickness of 0.6 mm was prepared and its compression performance was tested using a universal testing machine, ensuring a compression strain of 50%.

2.6. Solar-driven water evaporation test

A xenon lamp with model PLS-SXE 300+ equipped with a standard AM 1.5G filter was used to simulate the solar light source for the seawater desalination experiment. The intensity of the xenon lamp light source was detected using an optical power meter with model CEL-NP2000, and the light intensity was adjusted to 100 mW/cm^2. The size of the aerogel sample was 2 cm × 2 cm × 0.6 cm. Polyurethane foam was selected as the thermal insulation layer and placed in a glass dish filled with water, leaving a 2 cm × 2 cm hole in the middle to accommodate melamine foam as the water supply layer. FG/CNF aerogel was placed on the melamine foam for the experiment. The sample surface was preheated for 1 h before measuring the water evaporation rate. Prior to the evaporation rate measurement, the sample surface was preheated under simulated solar illumination for 1 h to ensure thermal equilibrium and stabilize the water transport within the scaffold. An electronic analytical scale (accurate to 0.1 mg) was used to monitor changes in water quality and record them in real-time. An infrared thermal imager (FLIR E3) was used to capture surface temperature and real-time images. The water evaporation rate was calculated according to the following formula:

$$\triangle V = \frac{m}{ST}$$

In the formula, ΔV represents the evaporation rate of water, m represents the mass change of water, S represents the area of light vertically irradiated on the sample, which corresponds to the full top surface of the Janus FG/CNF structure, including both solid and porous regions, as all areas are exposed to air and contribute to evaporation [33,34]. And T represents the illumination time.

2.7. Salt resistance performance test

A total of 0.5 g of NaCl was weighed and uniformly spread over the surface of the FG/CNF composite. The sample was then placed in a seawater desalination device, where the changes in surface NaCl were continuously monitored and recorded at regular intervals. FG/CNF was placed in an environment with a 15% concentration of NaCl under illumination, and whether salt crystals precipitate on its surface after 12 h was observed. Furthermore, NaCl solutions with concentrations of 5%, 10%, and 20% was prepared, and the change in evaporation rate of FG/CNF as the salt concentration increases was tested.

2.8. Water purification capability test

An acrylic-sealed device was used to capture the water vapor, and the FG/CNF composite's purification efficiency was evaluated in seawater, dye-contaminated solutions, and acidic and basic media. Subsequently, the concentrations of four main ions (Na^+, K^+, Mg^{2+}, Ca^{2+}) in water were measured using inductively coupled plasma optical emission spectrometry (ICP-OES). The ICP-OES has a detection range of 0–40 mg/L. For samples with concentrations exceeding this range, appropriate dilutions were performed to ensure measurement accuracy. Each sample was tested in triplicate, and the average values with standard deviations were reported. The absorbance of methylene blue and rhodamine B at 665 nm and 554 nm was measured using a UV–visible spectrophotometer (TU-1901). The pH change of the solution was measured using acid-base pH test strips.

2.9. Outdoor seawater desalination effect test

Nine FG/CNF arrays, each measuring 2 cm × 2 cm × 0.6 cm, were fabricated for outdoor experiments. An electronic balance was used to track mass changes, a humidity meter recorded the ambient humidity, an optical density meter measured light intensity, and an acrylic sealed box was employed to collect condensed water. The water evaporation rate of the samples was measured hourly from 9:20 to 17:20.

3. Results and discussion

The fabrication process of the Janus solar evaporator is shown in Fig. 1 and detailed in the Methods section. Flash graphene (FG) was synthesized using the Flash Joule Heating (FJH) technique, with carbon black as the precursor material (Vid. S1). This process, as described in previous studies, involves rapid heating to approximately 3000 K within ~1 ms using a custom-built FJH device. The resulting FG was then compounded with nano-cellulose to create a printable ink for 3D printing the Janus solar evaporator. Raman spectroscopy confirmed the successful synthesis of FG, showing D, G, and 2D characteristic peaks at 1348, 1577, and 2694 cm^{-1}, respectively, with a 2D/G value of approximately 0.82, indicating that graphene is of high quality [35] (Fig. S3). X-ray diffraction (XRD) revealed a distinct (002) peak and an asymmetric (100) peak (Fig. 2a), which are characteristics of turbo graphene [36]. Transmission electron microscopy (TEM) revealed that FG consists of hexagonal nanosheets, and high-resolution TEM confirmed a lattice spacing of 0.347 nm [37], corresponding to the (002) plane of graphitic carbon (Fig. 2b-c). The extreme reaction conditions of the FJH process produce unconventional turbostratic structures, which lack the typical A-B stacking of graphite. This unique structure contributes to the high exfoliation efficiency of FG, especially when combined with the commercial surfactant Pluronic F-188 [38,39]. The surfactant facilitates the homogeneous dispersion of FG in aqueous solutions at concentrations as low as 0.2 wt%. To highlight the exceptional dispersibility of FG, its aqueous dispersion was compared to that of graphene oxide (GO), a widely used hydrophilic graphene derivative. As shown in Fig. 2d, with the addition of Pluronic F-188, the FG solution remained stable even after 24 h, while the GO dispersion exhibited noticeable sedimentation within 2 h. This enhanced stability of FG can be attributed to its ultrafine size, approximately 10 nm, and its unique turbostratic structure. Moreover, unlike GO, which achieves water dispersibility through the introduction of oxygen-containing functional groups, FG retains its graphene structure without undergoing chemical oxidation. While GO reduction can regenerate its graphitic framework [40], such processes often distort the original graphene structure, potentially reducing photothermal efficiency. In contrast, FG combines high dispersibility with structural integrity, preserving its abundant sp^2 carbon network and superior photothermal properties [41]. To demonstrate this, a 0.2 wt% aqueous dispersion of FG was irradiated under 1-sun light, resulting in a stable increase in water temperature to approximately 42 °C (Fig. 2e-f). This temperature rise is sufficient to significantly enhance water vapor generation, highlighting FG's potential as an efficient photothermal material. FG's small size, excellent dispersibility and stability in aqueous solutions, and high photothermal efficiency at low concentrations make it a promising candidate for incorporation into 3D printing inks.

To effectively demonstrate the suitability of FG as a photothermal agent for the 3D-printed solar evaporator, cellulose-based printable ink was used as the model material [42]. Cellulose-based inks offer several advantages, including the ability to form highly porous and hydrophilic matrices, which promote water transport and evaporation. Furthermore, cellulose is an abundant, renewable, and environmentally friendly resource with intrinsic hydrophilicity, making it ideal for applications that require efficient water absorption and capillary action [43]. The preparation of the cellulose-based ink followed established methods from previous studies [44]. Cellulose nanofibers (CNF) are extracted from coniferous wood pulp, and the separated CNF measures approximately 4 nm in width (Fig. S4). CNF and carboxymethyl cellulose (CMC) were combined to form a printable solution, with citric acid (CA) added as a crosslinking agent. The ink's viscosity was adjusted by varying the water content to ensure optimal printability. Inks with solid contents of 10%, 12%, and 15% were evaluated for their rheological behavior, all showing high viscosity and a solid-like state, as demonstrated by their

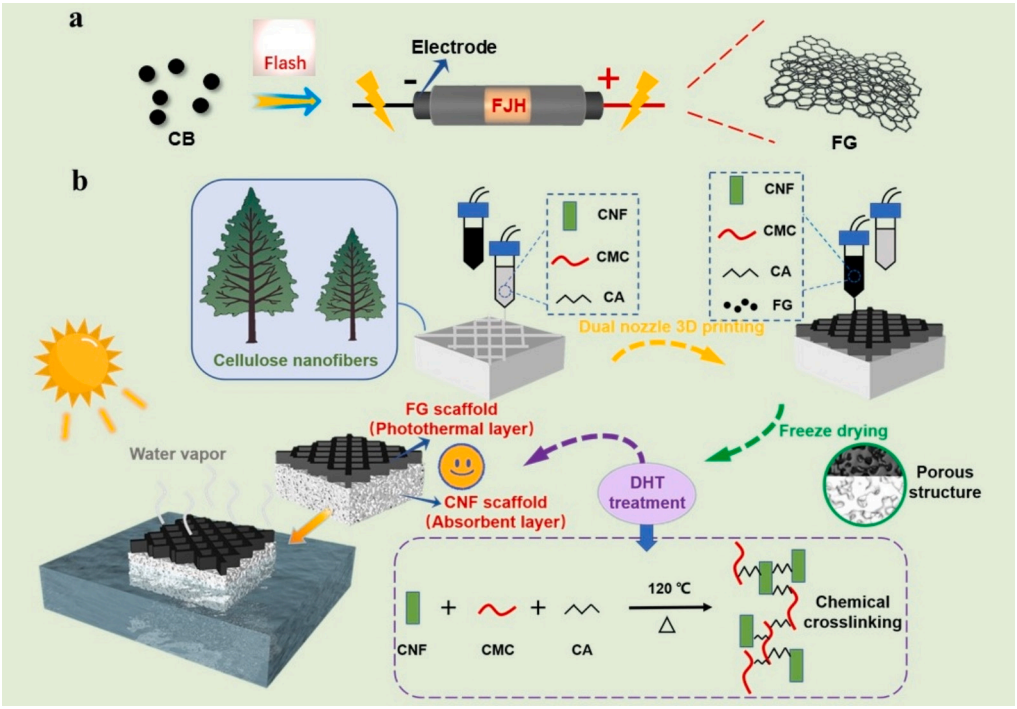

Fig. 1. Schematic diagram of a) FG preparation and b) Janus FG/CNF preparation.

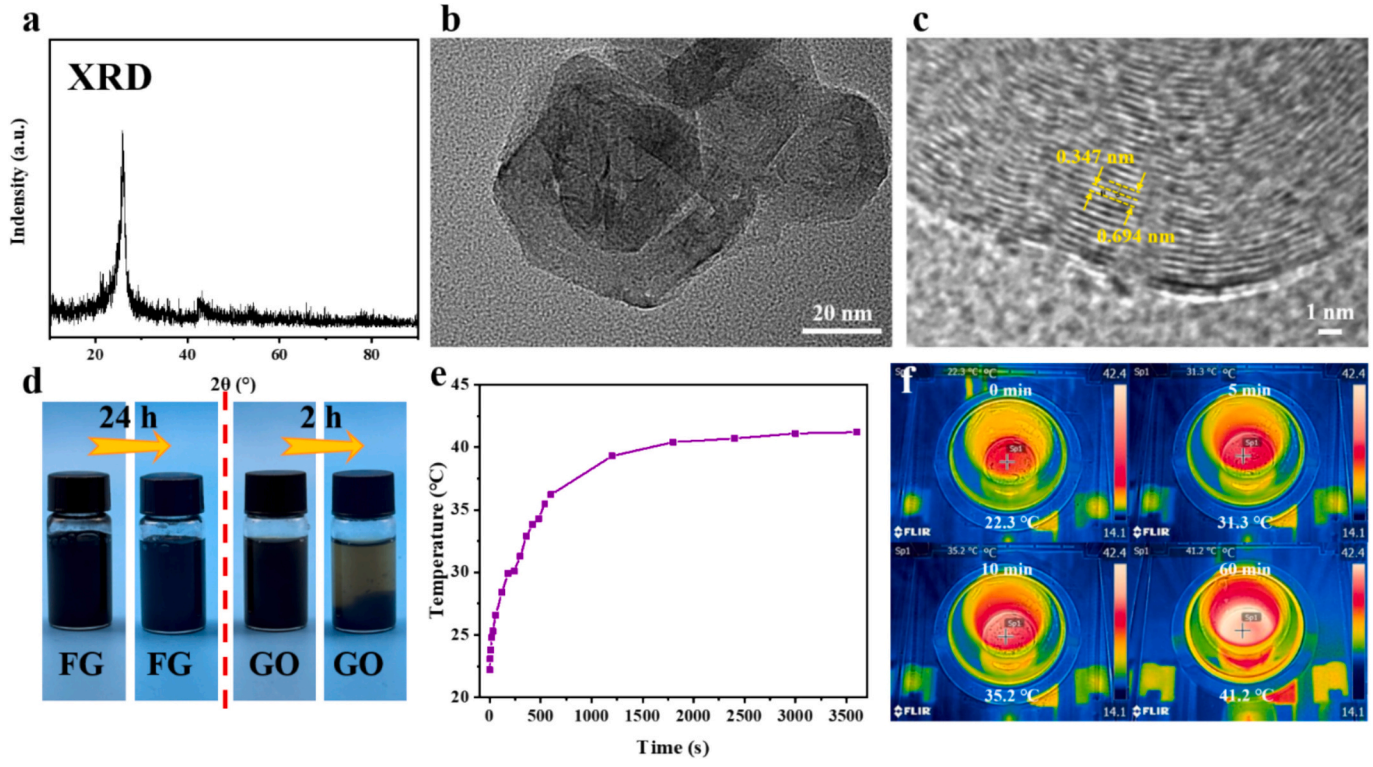

Fig. 2. a) XRD pattern, b) TEM image, c) High-resolution TEM of Flash graphene. d) Images demonstrating the dispersion stability of GO and FG in aqueous suspensions with added Pluronic F-188. e) Heating curve and f) infrared thermogram of FG solution.

stability in inverted glass bottles (Fig. 3a). However, as shown in Fig. 3b, inks with 10% and 12% solid content exhibited poor formability, with blurred boundaries in the printed lines. In contrast, the ink with 15% solid content displayed excellent printability, enabling continuous extrusion through the nozzle without interruption (Fig. S5). The resulting printed lines were smooth, well-defined, and maintained their shape, forming a precise grid structure. Furthermore, with optimized printing settings, including printing speed (6 mm/s), layer height (0.2 mm), nozzle diameter (260 μm), and applied pressure (0.24 MPa), the ink with 15% solid content successfully produced a 3D-printed pyramid model (Fig. 3c), demonstrating its versatility in constructing complex structures.

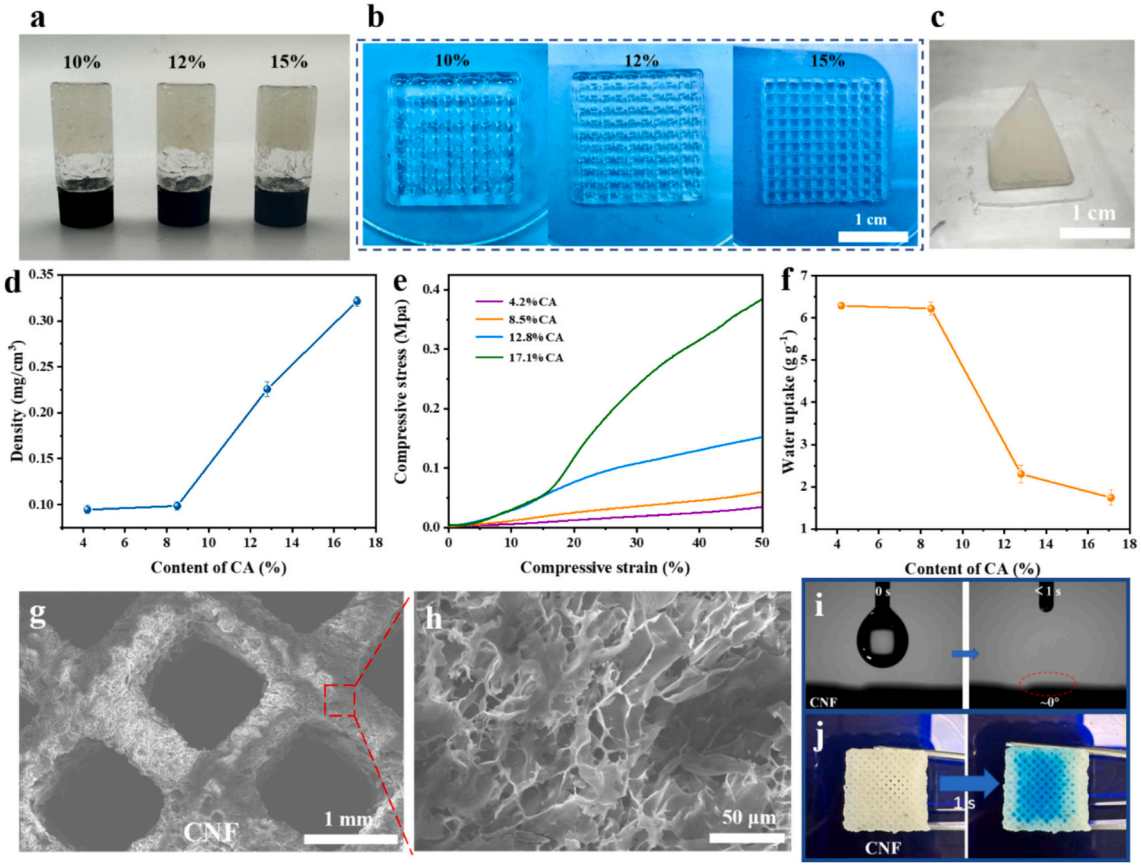

Fig. 3. a) Display photos of CNF ink viscosity with different solid contents. b) CNF printable schematic diagram. c) Photo of 3D printed pyramid. The d) density, e) compression performance (wet state), and f) water absorption of CNF scaffolds with different CA contents. g-h) SEM morphology images of the surface of CNF scaffolds. i) Contact angle test and j) water transport test of CNF scaffolds.

After printing, the CNF scaffold underwent freeze-drying to create a porous structure, followed by dehydrogenation heat treatment (DHT) at 120 °C to chemically crosslink the matrix. This solvent-free heat treatment promoted the formation of ester bonds between hydroxyl groups in CNF or CMC and carboxyl groups of citric acid (CA) [45]. Without the DHT treatment or the inclusion of CA, the scaffolds dissolved in water, confirming the importance of crosslinking for maintaining structural stability (Fig. S6). Following treatment, the scaffold's color changed from white to yellow as CA content increased (Fig. S7), likely due to CA dehydration and the formation of unsaturated acids. The density and mechanical properties of the aerogels were influenced by the CA concentration. As shown in Fig. 3d-e, higher CA concentrations resulted in denser aerogels with improved compressive strength, particularly after 50% compression strain in a wet state. However, this also reduced water absorption (Fig. 3f), likely due to tighter crosslinking between monomers that decreased porosity. For seawater desalination, a balance between structural integrity and water absorption is essential. A scaffold with 8.5 wt% CA provided an optimal balance and was selected for following experiments. The optimized 3D printed CNF scaffold showed good structural integrity after compression tests, as the scaffold maintained its shape and thickness (~0.6 cm) before and after 50% compression strain (Fig. S8). Combining the 3D printing technique with the freeze-drying method, the resulting CNF scaffold exhibits both macroscopic and microscopic structural features. As shown in Fig. 3g-h, the scaffold consists of 1.4 mm wick channels created through 3D printing and approximately 20 μm open microchannels in the aerogel, formed during the freeze-drying process. Due to its highly hydrophilic nature (Fig. 3i), the interconnected wick channels and microchannels enable efficient water transport (Fig. 3j). A water transportation experiment, depicted in Fig. S9, demonstrates this capability, where colored water rapidly moves from the bottom of the scaffold to dye the white paper on its top surface in less than one second. This rapid water transport will significantly enhance the timely delivery of water to the photothermal region and facilitates the fast diffusion of salt ions, both of which are essential for achieving high evaporation rates and maintaining long-term operational stability.

Next, we demonstrate that the addition of a small amount of FG to the cellulose ink imparts photothermal properties without compromising its printability or the properties of the resulting 3D-printed scaffold. The preparation of the FG/cellulose ink, along with its subsequent printing and post-processing, followed the same procedure as the pure cellulose ink, with the exception of adding 0.08 wt% FG. The concentration was selected based on its optimal photothermal and evaporation performance among the tested concentrations (Fig. S10). The inclusion of FG did not significantly alter the ink's printability. As shown in Fig. 4a, the FG/cellulose ink exhibited high viscosity, maintaining a solid-like state when inverted in a beaker. It also extruded smoothly through the nozzle without interruptions (Fig. 4b). Using identical printing parameters—including printing speed, layer height, nozzle diameter, and applied pressure—as those used for pure cellulose ink, the FG/cellulose ink demonstrated excellent printability and versatility. Various geometric patterns, such as CUG structures, fence-like grids, and Taiji Bagua motifs, were successfully printed (Fig. 4c), highlighting the compatibility of FG incorporation with precise and customizable 3D printing. Following freeze-drying and dehydrogenation heat treatment, the resulting FG/cellulose scaffolds retained the hierarchical porous structures observed in pure cellulose scaffolds (Fig. 4d-e). Notably, the addition of FG further improved pore uniformity and openness, as the FG nanosheets may acted as spacers that reduced fibril aggregation and helped stabilize the 3D porous network during drying.

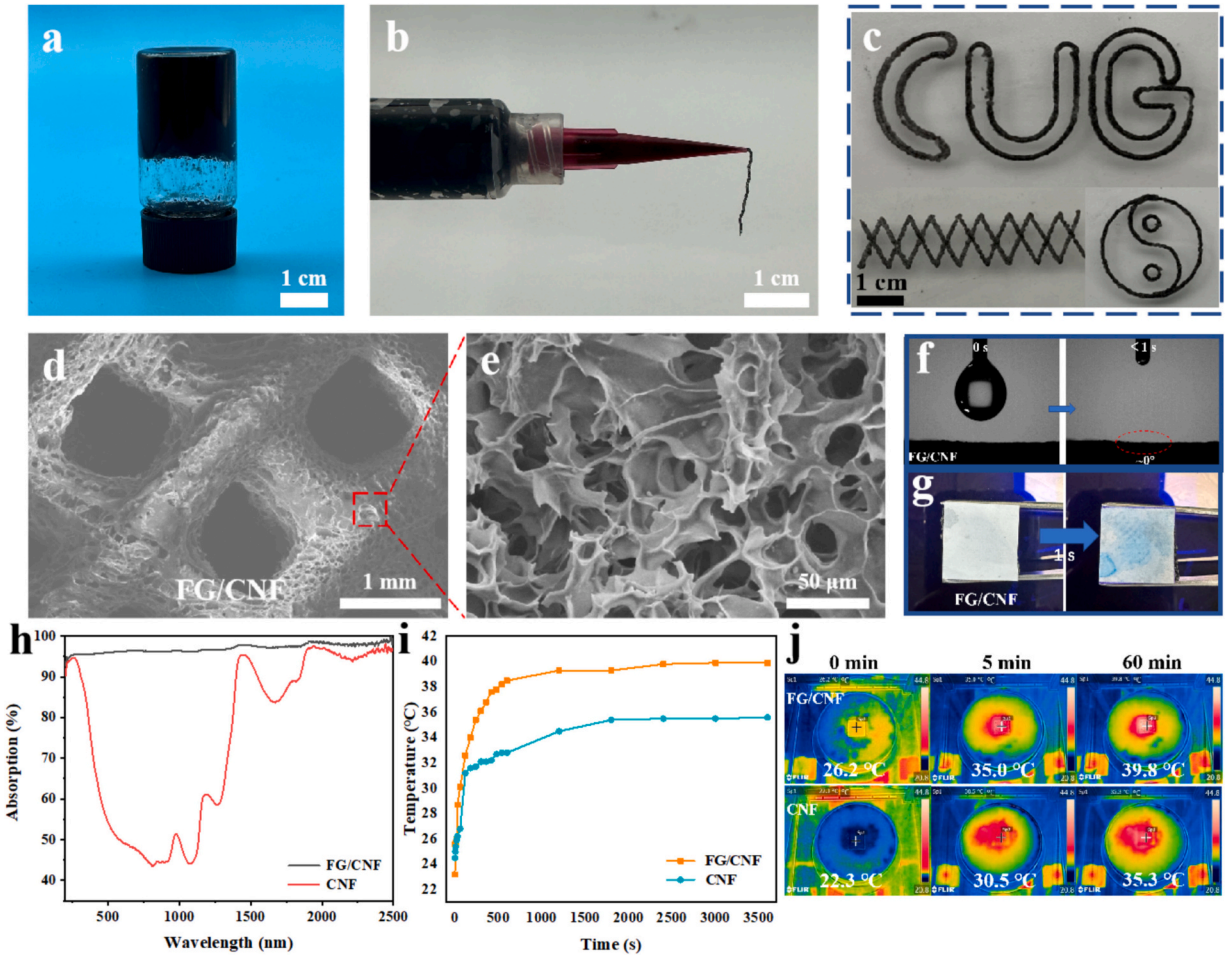

Fig. 4. a) Display photos of FG ink's viscosity. b) Photos of ink extrusion. c) Photos of FG ink printed graphics. d, e) SEM image of FG/CNF scaffold's surface. f) Contact angle test and g) water transport test of FG/CNF scaffolds. h) UV–Vis-NIR spectra of FG/CNF and CNF. i) The temperature rise curve of different aerogels (wet state). j) Infrared thermography of different aerogels.

This similarity can be attributed to the minimal concentration of FG, its nanoscale size (~10 nm), and its high dispersibility in aqueous solutions, which together minimize disruption to the microstructure and ensure consistency in printability. Additionally, the surface hydrophilicity, water transportation and compression resistance properties of FG/cellulose scaffolds were comparable to those of pure cellulose scaffolds (Fig. 4f-g, Fig. S11), maintaining their suitability for solar desalination applications. Despite the minimal addition of FG, the FG/cellulose scaffolds exhibited superior photothermal performance due to FG's exceptional light absorption and photothermal conversion efficiency. As shown in Fig. 4h, the FG/cellulose scaffold achieved a high light absorption efficiency of 96.98%, significantly surpassing the performance of pure cellulose scaffolds. This enhancement enabled efficient photothermal conversion, with the FG/cellulose scaffold floating on water stably reaching approximately 40 °C after 60 min of irradiation under one-sun light. In contrast, the pure cellulose scaffold only achieved a temperature of 35 °C under the same conditions. This notable improvement in thermal performance confirms the effectiveness of FG as a photothermal agent (Fig. 4i-j). The enhanced photothermal properties of the FG/cellulose scaffold, combined with its preserved printability and structural integrity, highlight the potential of FG as a functional additive for advanced solar evaporators.

Given the similar printability of both the pure cellulose ink and the FG/cellulose ink, and since both inks share cellulose-based materials as their primary matrix, multi-material 3D printing was used to fabricate a Janus-structured FG/cellulose aerogel-based solar evaporator (Vid. S2). Notably, the resulting FG/CNF aerogel has a low density of 22.5 mg, comparable to previously reported aerogels [46,47], and demonstrates its lightness by resting intact on a flower (Fig. 5a). The Janus design features a photothermal layer atop a hierarchical porous scaffold, with strong interfacial bonding (Fig. S12) ensuring structural stability. This configuration optimizes heat localization while preventing direct contact between the photothermal layer and cooler water, thereby improving solar energy utilization efficiency [20,28]. As a result, the Janus FG/CNF evaporator exhibited a significantly improved photothermal effect compared to the FG/CNF evaporator. Thermal imaging measurements under identical experimental conditions (evaporators floating on water and irradiated by one-sun light) revealed that the top surface temperature of the Janus FG/CNF evaporator was substantially higher at 45 °C, compared to 39.8 °C for the FG/CNF evaporator (Fig. 5b-c). To further assess heat localization, side-view thermal images of the evaporators were captured (Fig. 5d-e). The Janus FG/CNF evaporator demonstrated strong heat localization, with elevated temperatures concentrated at the top FG layer. In contrast, the FG/CNF evaporator exhibited a gradient heat distribution, with faster heat dissipation towards the water layer. These observations highlight the efficacy of the Janus design in minimizing heat loss and maximizing thermal efficiency.

Then, the solar evaporation experiments were conducted using the setup shown in Fig. 5f, where the evaporator samples were placed on melamine foam covered with thermal insulation foam. A glass dish filled with water was irradiated by a xenon lamp to simulate sunlight. An electronic balance continuously monitored mass changes to determine evaporation rates. The FG/CNF evaporator achieved a high evaporation

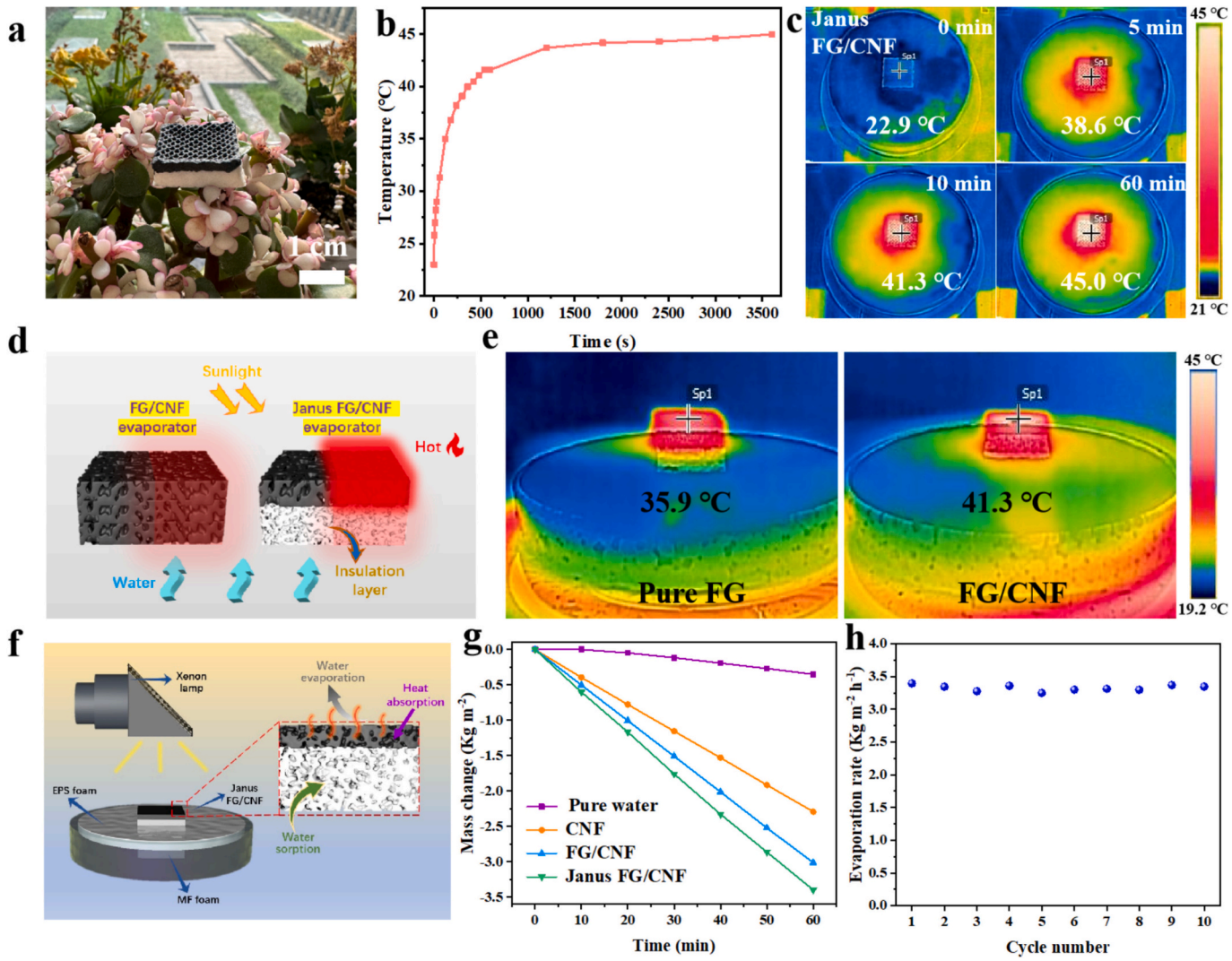

Fig. 5. a) Photos showcasing the lightweight features of the Janus FG/CNF. b) The temperature rise curve of the Janus FG/CNF aerogel (wet state). c) Infrared thermography of the Janus FG/CNF aerogel. d) Schematic diagram of heat distribution under illumination. e) Infrared thermal imaging of temperature distribution on the cross-section (The thermal imaging instrument detected a temperature difference of about 4 °C between the section near the surface and the actual surface temperature). f) Diagram of photothermal seawater desalination device. g) Mass change of different aerogels structure with illumination time. h) Circulating evaporation performance.

rate of 3.0 kg m^{-2} h^{-1}, significantly exceeding the evaporation rate of pure water (0.35 kg m^{-2} h^{-1}). This enhanced performance can be attributed to FG's superior photothermal properties and the scaffold's hierarchical structure, which includes the cellulose scaffold's inherent porosity and the interconnected wick channels formed during 3D printing. These features promote rapid water delivery and transport, contributing to the evaporator's high efficiency. The evaporation performance was further improved by incorporating the Janus design through multi-material 3D printing. The Janus FG/CNF evaporator exhibited an evaporation rate of 3.397 kg m^{-2} h^{-1}, surpassing the FG/CNF evaporator and most previously reported results for hydrogel- or aerogel-based solar evaporators (Fig. 5g, Table S1). This enhanced performance highlights the Janus structure's ability to optimize heat localization and solar energy utilization effectively. Based on Eq. S1, the photothermal conversion efficiency of the Janus FG/CNF evaporator was calculated to be as high as 229%. It is worth noting that a photothermal conversion efficiency exceeding 100% results from the reduced effective evaporation enthalpy within the porous hydrophilic matrix. This phenomenon is commonly observed in hydrogel- and aerogel-based evaporators, where strong water–matrix interactions and interfacial evaporation effects enable water evaporation with lower energy input than that required for bulk water [48–51]. In addition to its high evaporation efficiency, the 3D-printed Janus FG/CNF evaporator demonstrated excellent cycling stability. Over six evaporation cycles, the evaporator maintained consistent performance, as shown in Fig. 5h. Morphological analysis of the Janus scaffold after prolonged exposure to light and multiple cycles of water evaporation (Fig. S13) revealed no significant structural shrinkage or collapse. The scaffold retained its original integrity and grid structure even after 6 and 12 h of solar-driven desalination. These findings confirm the exceptional structural stability and durability of the 3D-printed Janus FG/CNF evaporator, making it a reliable solution for sustainable seawater desalination applications.

The 3D-printed Janus FG/CNF evaporator, with its hierarchical porous structure, effectively optimizes the scaffold design for both rapid water supply and efficient salt circulation. This structural advantage significantly reduces salt accumulation during prolonged sunlight exposure. The evaporator demonstrated exceptional resistance to salt accumulation and self-cleaning capabilities. When 0.5 g of solid NaCl was placed directly on the upper surface of the evaporator, it completely dissolved within 110 min under sunlight exposure (Fig. 6a). This process is facilitated by the interconnected porous network within the scaffold, as shown schematically in Fig. 6b. Capillary-driven transport connects

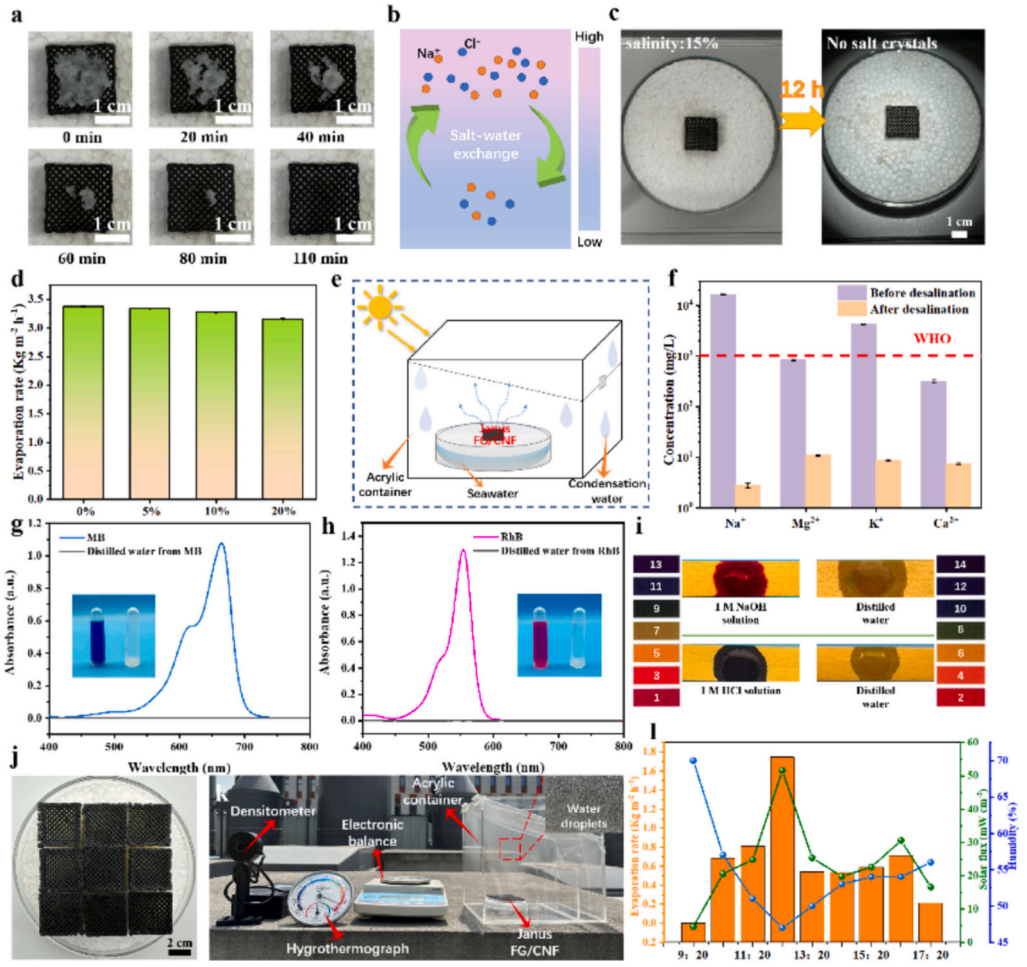

Fig. 6. a) Display photos of salt dissolution. b) Schematic diagram of salt water exchange. c) Surface morphology of evaporator after 12 h of evaporation in 15% saline solution. d) Evaporation rate in solutions of different salt concentrations. e) Water purification device diagram. f) The ion concentration of seawater before and after desalination. UV visible absorption spectra of g) MB and h) RhB before and after simulated wastewater purification. i) The pH value of the acidic/alkaline aqueous solution before and after purification. j) Photos of the Janus FG/CNF array. k) Photos of outdoor experimental equipment. l) The variation chart of outdoor light intensity, humidity and evaporation rate over time.

the evaporation interface to the bulk water, enabling the diffusion and convection of salt ions from areas of high concentration to the surrounding low-salinity water. This creates a concentration gradient that promotes salt migration and prevents surface deposition. Moreover, after 12 h of sunlight exposure in a 15 wt% NaCl solution, no solid salt residue was observed on the evaporator's surface (Fig. 6c). The presence of large pores and continuous water supply ensures consistent evaporation performance, even at high salinity levels. The evaporation rate showed only a slight decrease with increasing salinity (Fig. 6d), primarily due to the reduced saturated vapor pressure associated with higher NaCl concentrations. These results highlight the evaporator's strong salt resistance, making it highly suitable for seawater photothermal evaporation.

To further assess the FG/CNF evaporator's capabilities, purification tests were conducted on simulated seawater, dye wastewater, and acid-base solutions. The setup shown in Fig. 6e was used to collect condensate water during desalination experiments. For seawater purification, ion concentrations of Na^{+}, Mg^{2+}, K^{+}, and Ca^{2+} were significantly reduced from initial levels of 16,392.64, 842.08, 4257.27, and 314.33 mg/L, respectively, to 2.82, 10.87, 8.7, and 7.48 mg/L—well below the WHO drinking water standards for ion content (Fig. 6f). These results confirm the feasibility of using the Janus FG/CNF evaporator for seawater desalination. The evaporator's performance was then tested using methylene blue (MB) and rhodamine B (RhB) dye solutions to simulate industrial dye wastewater. The collected condensate was transparent, and UV–visible absorption spectra (665 nm for MB and 554 nm for RhB) showed no absorption peaks corresponding to the dye molecules (Fig. 6g-h). This indicates nearly complete removal of the dye molecules, confirming the evaporator's effectiveness for dye wastewater treatment. The evaporator also demonstrated excellent purification performance for acid-base wastewater. Post-desalination pH measurements of the collected water, using pH test strips, consistently indicated neutral pH values of approximately 7 (Fig. 6i). These results demonstrate that the FG/CNF evaporator can produce safe drinking water, highlighting its versatility for various wastewater treatment applications. To further evaluate the evaporator's practical performance in seawater desalination, a full-day outdoor test was conducted from 9:20 to 17:20. A 6 cm × 6 cm evaporator array (Fig. 6j) was used in the experimental setup shown in Fig. 6k. Environmental parameters such as light intensity, humidity and mass changes were recorded hourly using a densitometer, hygrometer, and electronic balance. The produced steam was collected in an acrylic sealed box, where condensation droplets on the walls indicated successful desalination. As shown in Fig. 6l, the highest sunlight intensity occurred at 12:20, corresponding to lowest relative humidity, and the highest recorded evaporation rate. These findings underscore the evaporator's robust performance under real-world conditions.

4. Conclusion

In this study, a 3D-printed flash graphene (FG) composite nanocellulose aerogel (CNF) was successfully developed for solar evaporation applications, achieving high evaporation efficiency and excellent salt resistance. The cellulose-based ink, enhanced with a small amount of FG, demonstrated superior printability and structural integrity, enabling the fabrication of versatile geometries and hierarchical porous scaffolds. The incorporation of FG endowed the aerogel with remarkable photothermal properties, achieving a light absorption efficiency of 96.98% and a significant temperature increase under solar irradiation. The Janus-structured FG/CNF evaporator, fabricated via multi-material 3D printing, exhibited enhanced heat localization, which improved solar energy utilization and resulted in a high evaporation rate of 3.397 kg m^{-2} h^{-1}. Its hierarchical porous structure facilitated rapid water transport and salt diffusion, effectively mitigating salt accumulation and ensuring sustained performance in high-salinity environments. The evaporator also demonstrated exceptional purification capabilities, producing potable water from seawater, dye-laden wastewater, and acid-base solutions. Furthermore, outdoor desalination tests confirmed its practical applicability for large-scale freshwater production. These findings highlight the potential of the FG/CNF aerogel as a robust and sustainable solution for solar-driven water desalination and purification.

Supplementary data to this article can be found online at https://doi.org/10.1016/j.cej.2025.165496.

CRediT authorship contribution statement

Zhigang Wang: Writing – review & editing, Writing – original draft, Investigation, Data curation, Conceptualization. **Chunjie Yan:** Supervision, Formal analysis. **Kaiyue Ji:** Visualization, Data curation. **Jun Cao:** Visualization, Data curation. **Yang Chen:** Visualization. **Yuting Gao:** Visualization. **Heng Deng:** Writing – review & editing, Supervision, Funding acquisition, Conceptualization.

Declaration of competing interest

The authors declare that they have no known competing financial interests or personal relationships that could have appeared to influence the work reported in this paper.

Acknowledgments

The work was supported by Guangdong Basic and Applied Basic Research Foundation (No. 2022A1515110026) and National Natural Science Foundation of China (No. 52303163). The project was supported by the “CUG Scholar” ScientificResearch Funds at China University of Geosciences (Wuhan) (Project No.2021175).

Data availability

Data will be made available on request.

References

[1] S. Xu, A.J. Hutchinson, M. Taheri, B. Corry, J.F. Torres, Thermodiffusive desalination, Nat. Commun. 15 (1) (2024) 2996.
[2] Z. Huang, J. Wei, Y. Wan, P. Li, J. Yu, J. Dong, S. Wang, S. Li, C.S. Lee, Aligned Millineedle arrays for solar power seawater desalination with site-specific salt formation, Small 17 (43) (2021) e2101487.
[3] M. Ding, D. Zhao, H. Liu, Y. Zhao, F. Li, D. Jia, C. Li, Ink-stained chalk: a low-cost 3D evaporator for efficient and stable solar desalination, Sol. RRL 7 (9) (2023) 2300026.
[4] Y. Zhang, S. Wang, D. Han, H. Chen, H. Liu, J. Zhu, W. Luo, C. Shi, Y. Song, Z. Ling, 3D macroporous MXene/sodium alginate aerogels with “brick-concrete” structures for highly efficient solar-driven water purification, Desalination 585 (2024).
[5] R. Ding, Y. Meng, Y. Qiao, M. Wu, H. Ma, B. Zhang, Functionalizing cotton fabric via covalently grafting polyaniline for solar-driven interfacial evaporation of brine, Appl. Surf. Sci. 598 (2022).
[6] M. Ding, D. Zhao, R. Wei, Z. Duan, Y. Zhao, Z. Li, T. Lin, C. Li, Multifunctional Elastomeric Composites Based on 3D Graphene Porous Materials, Wiley Online Library, Exploration, 2024, 20230057.
[7] Y. He, D. Zhao, H. Wang, X. Gong, M. Ding, Z. Duan, T. Lin, R. Wei, J. Liu, C. Li, 3D graphene composite foams for efficient and stable solar desalination of high-salinity brine, Sol. RRL 7 (14) (2023) 2300313.
[8] S. Yang, Y. He, J. Bai, J. Zhang, Synergistic dual-mechanism localized heat channeling and Spectrum-tailored liquid metal hydrogels for efficient solar water evaporation and desalination, Small 19 (43) (2023) e2302526.
[9] Q. Zhu, K. Ye, W. Zhu, W. Xu, C. Zou, L. Song, E. Sharman, L. Wang, S. Jin, G. Zhang, Y. Luo, J. Jiang, A hydrogenated metal oxide with full solar Spectrum absorption for highly efficient Photothermal water evaporation, J. Phys. Chem. Lett. 11 (7) (2020) 2502–2509.
[10] Y. Li, P. Liu, Y. Gao, Y. Feng, P. Li, X. Chen, Scattered co-anchored MoS2 synergistically boosting photothermal capture and storage of phase change materials, journal of energy, Chemistry 95 (2024) 208–215.
[11] D.A.R.O. da Silva, L.C.B. Zuge, A. de Paula Scheer, Pretreatments for seawater desalination by pervaporation using the developed green silica/PVA membrane, J. Environ. Chem. Eng. 9 (6) (2021).
[12] J. Li, Z. Chen, H. Du, M. Xia, T. Yang, Q. Chen, L. LV, D. Wang, J. Xiao, 3D-printed flower-inspired evaporator for simultaneous solar seawater desalination and hydrogen production, Chem. Eng. J. 515 (2025) 163629.
[13] R. Zhao, X. Chen, X. Chen, P. Zhang, C. Luo, P. Zhang, M. Chao, L. Yan, A self-healing, deformation-resistant MXene double-network hydrogel for stable solar-driven interfacial evaporation, J. Mater. Chem. A 13 (2025) 5684–5693.
[14] R. Zhu, D. Wang, J. Xie, Y. Liu, M. Liu, S. Fu, Salt-resistant Schiff base cross-linked superelastic photothermal cellulose aerogels for long-term seawater desalination, Chem. Eng. J. 427 (2022).
[15] M. Tang, C. Qi, L. Yue, Cu-Fe3O4/sodium alginate/polyacrylamide hydrogel evaporator for solar seawater desalination, Sol. Energy Mater. Sol. Cells 278 (2024).
[16] Y. Xu, B. Lv, Y. Yang, X. Fan, Y. Yu, C. Song, Y. Liu, Facile fabrication of low-cost starch-based biohydrogel evaporator for efficient solar steam generation, Desalination 517 (2021) 115260.
[17] W.R. Cui, C.R. Zhang, R.P. Liang, J. Liu, J.D. Qiu, Covalent organic framework sponges for efficient solar desalination and selective uranium recovery, ACS Appl. Mater. Interfaces 13 (27) (2021) 31561–31568.
[18] H. Liu, D. Tian, Z. Zheng, X. Wang, Z. Qian, MXene-decorated magnetic phase-change microcapsules for solar-driven continuous seawater desalination with easy salt accumulation elimination, Chem. Eng. J. 458 (2023).
[19] M. Ding, D. Zhao, Z. Duan, Z. Pan, C.-Y. Liu, C. Li, J. Zhang, Bio-inspired solar evaporators for stable and efficient desalination of high-salinity brine with zero liquid discharge, Sci. Bull. (2025).
[20] H. Ma, L. Yu, Z. Li, J. Chen, J. Meng, Q. Song, Y. Liu, Y. Wang, Q. Wu, M. Miao, C. Zhi, A Lotus seedpods-inspired interfacial solar steam generator with outstanding salt tolerance and mechanical properties for efficient and stable seawater desalination, Small 19 (52) (2023) e2304877.
[21] P. Imrie, J. Jin, Multimaterial hydrogel 3D printing, Macromol. Mater. Eng. 309 (2) (2023).
[22] J. Yuan, X. Lei, C. Yi, H. Jiang, F. Liu, G.J. Cheng, 3D-printed hierarchical porous cellulose/alginate/carbon black hydrogel for high-efficiency solar steam generation, Chem. Eng. J. 430 (2022).
[23] P.D. Nguyen, T.Q. Nguyen, Q.B. Tao, F. Vogel, H. Nguyen-Xuan, A data-driven machine learning approach for the 3D printing process optimisation, Virtual Phys. Prototyp. 17 (4) (2022) 768–786.
[24] S. Geng, Q. Luo, K. Liu, Y. Li, Y. Hou, W. Long, Research status and prospect of machine learning in construction 3D printing, Case Studies in Construction Materials 18 (2023).
[25] Z. Lin, X. Qiu, Z. Cai, J. Li, Y. Zhao, X. Lin, J. Zhang, X. Hu, H. Bai, High internal phase emulsions gel ink for direct-ink-writing 3D printing of liquid metal, Nat. Commun. 15 (1) (2024) 4806.
[26] M. Pandey, K. Deshmukh, A. Raman, A. Asok, S. Appukuttan, G.R. Suman, Prospects of MXene and graphene for energy storage and conversion, Renew. Sust. Energ. Rev. 189 (2024).
[27] J. Tao, N. Arshad, M.S. Irshad, M. Alomar, F. Zhu, S. Huang, S. Zhai, V.-D. Dao, X. Wang, Tailorable MBene aerogel with the lowest evaporation enthalpy for solar seawater desalination and wastewater purification, Chem. Eng. J. 498 (2024).
[28] S. Zhang, M. Li, C. Jiang, D. Zhu, Z. Zhang, Cost-effective 3D-printed bionic hydrogel evaporator for stable solar desalination, Adv Sci (Weinh) 11 (17) (2024) e2308665.
[29] P.A. Advincula, W. Meng, J.L. Beckham, S. Nagarajaiah, J.M. Tour, Conversion of CO2-derived amorphous carbon into flash graphene additives, Macromol. Mater. Eng. 309 (2) (2023).
[30] K.M. Wyss, D.X. Luong, J.M. Tour, Large-scale syntheses of 2D materials: flash joule heating and other methods, Adv. Mater. 34 (8) (2022) e2106970.
[31] D.X. Luong, K.V. Bets, W.A. Algozeeb, M.G. Stanford, C. Kittrell, W. Chen, R. V. Salvatierra, M. Ren, E.A. McHugh, P.A. Advincula, Gram-scale bottom-up flash graphene synthesis, Nature 577 (7792) (2020) 647–651.
[32] Y. Chen, Z. Liu, Z. Wang, Y. Yi, C. Yan, W. Xu, F. Zhou, Y. Gao, Q. Zhou, C. Zhang, Bioinspired robust gas-permeable on-skin electronics: armor-designed Nanoporous flash graphene assembly enhancing mechanical resilience, Advanced Science 11 (26) (2024) 2402759.
[33] X. Zhou, M. Guo, M. Huang, Y. Xu, M. Liu, 3D printing of porous ceramic scaffold based halloysite clay for efficient seawater desalination, Chem. Eng. J. 501 (2024) 157659.

[34] S. Zhang, M. Li, C. Jiang, D. Zhu, Z. Zhang, Cost-effective 3D-printed bionic hydrogel evaporator for stable solar desalination, Adv. Sci. 11 (17) (2024) 2308665.
[35] C. Wang, B. Wang, X. Su, R. He, Synthesis of graphene from waste rubber powder based on flash joule heating method and its influence on the performance of cement mortar, Constr. Build. Mater. 451 (2024).
[36] P.A. Advincula, D.X. Luong, W. Chen, S. Raghuraman, R. Shahsavari, J.M. Tour, Flash graphene from rubber waste, Carbon 178 (2021) 649–656.
[37] Y.J. Xia-Hou, Y. Yu, J.R. Zheng, J. Yi, J. Zhou, T.X. Qin, E.M. You, H.L. Chen, S. Y. Ding, L. Zhang, K.L. Chang, K. Chen, M. Moskovits, Z.Q. Tian, Graphene coated dielectric hierarchical nanostructures for highly sensitive broadband infrared sensing, Small 19 (8) (2023) e2206167.
[38] W.A. Algozeeb, P.E. Savas, D.X. Luong, W. Chen, C. Kittrell, M. Bhat, R. Shahsavari, J.M. Tour, Flash graphene from plastic waste, ACS Nano 14 (11) (2020) 15595–15604.
[39] K.M. Wyss, W. Chen, J.L. Beckham, P.E. Savas, J.M. Tour, Holey and wrinkled flash graphene from mixed plastic waste, ACS Nano 16 (5) (2022) 7804–7815.
[40] V. Agarwal, P.B. Zetterlund, Strategies for reduction of graphene oxide – a comprehensive review, Chem. Eng. J. 405 (2021).
[41] X. Hu, D. Zuo, S. Cheng, S. Chen, Y. Liu, W. Bao, S. Deng, S.J. Harris, J. Wan, Ultrafast materials synthesis and manufacturing techniques for emerging energy and environmental applications, Chem. Soc. Rev. 52 (3) (2023) 1103–1128.
[42] C. Radeke, R. Pons, M. Mihajlovic, J.R. Knudsen, S. Butdayev, P.J. Kempen, C. P. Segeritz, T.L. Andresen, C.K. Pehmoller, T.E. Jensen, J.U. Lind, Transparent and cell-guiding cellulose nanofiber 3D printing bioinks, ACS Appl. Mater. Interfaces 15 (2) (2023) 2564–2577.
[43] K. Keeratipinit, P. Wijaranakul, W. Wanmolee, B. Hararak, Preparation of high-toughness cellulose nanofiber/Polylactic acid bionanocomposite films via gel-like cellulose nanofibers, ACS Omega 9 (24) (2024) 26159–26167.
[44] A.D. Stiglic, F. Gurer, F. Lackner, D. Bracic, A. Winter, L. Gradisnik, D. Makuc, R. Kargl, I. Duarte, J. Plavec, U. Maver, M. Beaumont, K.S. Kleinschek, T. Mohan, Organic acid cross-linked 3D printed cellulose nanocomposite bioscaffolds with controlled porosity, mechanical strength, and biocompatibility, iScience 25 (5) (2022) 104263.
[45] A. Dobaj Stiglic, F. Lackner, C. Nagaraj, M. Beaumont, M. Bracic, I. Duarte, V. Kononenko, D. Drobne, B. Madhan, M. Finsgar, R. Kargl, K. Stana Kleinschek, T. Mohan, 3D-printed collagen-Nanocellulose hybrid bioscaffolds with tailored properties for tissue engineering applications, ACS Appl. Bio Mater. 6 (12) (2023) 5596–5608.
[46] H. Wang, Z. Chen, D. Su, Lightweight and large-scale rGO reinforced SiBCN aerogels with hierarchical cellular structures exposed to high-temperature environments, J. Mater. Sci. Technol. 179 (2024) 145–154.
[47] K. Zhang, C. Li, L. Liu, X. Wang, N. Li, C. Yang, Y. Huang, H. Lu, H. Liu, J. Li, Developing lightweight silanized cellulose ultramaterials as the strongest engineered aerogel, Adv. Funct. Mater. 35 (9) (2025) 2415963.
[48] Y. Wang, Z. Cheng, W. Li, X. Zhao, S. Li, C. Cheng, A. Thomas, Y. Liao, Ginseng-bioinspired 3D Photothermal evaporator for efficient seawater desalination using conjugated microporous polymer, Advanced Sustainable Systems 8 (9) (2024) 2400142.
[49] L. Fu, X. Zhou, L. Deng, M. Liao, S. Chen, H. Wang, L. Wang, Carbonized waste polyphenylene sulfide non-woven decorated wood evaporator for clean water production from solar photothermal desalination, Desalination 550 (2023) 116362.
[50] N. Sen, A. Debnath, S. Bhattacharjee, B.K. Das, M. Thakur, A.K. Saha, K. K. Chattopadhyay, Efficient light to heat conversion in Sb2Se3 Nanorods and the role of macro-channel imprinted Sb2Se3 loaded hybrid membrane for superior desalination performance, Small 21 (7) (2025) 2408293.
[51] M. Ding, D. Zhao, P. Feng, B. Wang, Z. Duan, R. Wei, Y. Zhao, C.Y. Liu, C. Li, Highly efficient three-dimensional solar evaporator for zero liquid discharge desalination of high-salinity brine, Carbon Energy 6 (9) (2024) e548.